Energy 109 (2016) 378–390

Contents lists available at ScienceDirect

Energy

journal homepage: www.elsevier.com/locate/energy

Peak-power control of a grid-integrated oscillating water column wave energy converter

J.C.C. Henriques [a, *], L.M.C. Gato [a], J.M. Lemos [b], R.P.F. Gomes [a], A.F.O. Falcão [a]

[a] LAETA, IDMEC, Instituto Superior Técnico, Universidade de Lisboa, Av. Rovisco Pais, 1049-001 Lisboa, Portugal
[b] INESC-ID, Instituto Superior Técnico, Universidade de Lisboa, Rua Alves Redol 9, 1000-029 Lisboa, Portugal

ARTICLE INFO

Article history:
Received 13 December 2015
Received in revised form
2 April 2016
Accepted 22 April 2016
Available online 23 May 2016

Keywords:
Wave energy
Oscillating water column
Latching control
Peak-to-average power ratio control
OWC spar-buoy

ABSTRACT

A critical characteristic of most WECs (wave energy converters) is the large peak-to-average power ratio. This poses many challenges to the design of high-efficient PTO (power take-off) systems and, even more importantly, to integrate this form of renewable energy into power grids. The OWC (oscillating water column) WECs are devices whose PTO uses an air turbine as the primary energy converter. Besides its inherent simplicity, probably the greatest advantage of OWC based WECs is the ability to control or dissipate any excess of energy available to the PTO system that may occur in medium to highly energetic sea states. The contribution of the paper is the performance assessment of a new control algorithm to operate a HSSV (high-speed stop valve) installed in series with the turbine. The goal is to perform close-to-optimal latching control of the WEC and, simultaneously, operate the HSSV to limit the energy available to the turbine/generator set. The proposed control algorithm shows large improvements in the extracted mean power while limiting the peak-to-average power ratio, thus improving the power quality delivered to the electrical grid. Tests performed in a large-scale PTO test rig validated the algorithm.

1. Introduction

The European Strategy for Energy and Climate change has defined a set of action plans for the reduction of greenhouse gases. One of those actions imposes that 20% of energy consumption has to originate from renewable sources by 2020, a value still far from its objective [1,2]. Energy security issues are also forcing the EU (European Union) to focus on the investment of innovative renewable energy technologies [3]. However, the large integration of renewable is only possible through the diversification of energy sources [4–6]. The ocean waves are known to be an abundant energy source, but the technology for their conversion is still far from fully mature [7,8]. Because of that, the EU is creating policy mechanisms to raise the competitiveness of the wave energy industry to the level of the more conventional renewable technologies [9].

The hydrodynamic performance and the integration of the power take-off system, especially under extreme wave conditions are critical issues [10–12]. A characteristic of most WECs (wave energy converters) is the randomness and the large peak-to-average ratio of the power output under irregular waves. Yet few works have been devoted to the integrated study of the hydrodynamics and the control of the turbine-generator set.

For grid operators, the integration of this new form of renewable energy – the wave energy with its unique specific features – introduces new challenges that have to be addressed. In most devices, peak-to-average power ratio control – peak shaving – is a difficult task due to the limited capability of the power take-off system to control or dissipate the excess of energy that occurs in the more energetic sea states.

Normal operation under medium to more energetic sea states requires a PTO system with an oversized generator. This choice has two main drawbacks: i) it increases the PTO costs and, most importantly, ii) it reduces the produced energy due to the inherent low efficiency of the generator/power converter set under small load operation.

The OWC (oscillating-water-column) devices are possibly the systems in which the control of the peak-to-average power ratio can be more easily and more effectively achieved. In an OWC, there is a fixed or floating hollow structure, open to the sea below the water surface, that traps air above the inner free-surface [13]. Wave

* Corresponding author. Tel.: +351 218 417 927.
E-mail addresses: joaochenriques@tecnico.ulisboa.pt (J.C.C. Henriques), luis.gato@tecnico.ulisboa.pt (L.M.C. Gato), jlml@inesc.pt (J.M. Lemos), ruigomes@tecnico.ulisboa.pt (R.P.F. Gomes), antonio.falcao@tecnico.ulisboa.pt (A.F.O. Falcão).

http://dx.doi.org/10.1016/j.energy.2016.04.098
0360-5442/

Nomenclature

Romans
- a constant of the generator control law (22)
- $\mathbf{A}_{ij}$ state matrix of the radiation R_{ij} [s^{-1}] state-space representation (5)
- A_{ij}^{∞} limiting value at infinite frequency of [kg] the added mass of body i as affected by body j motion
- A_{ω} wave amplitude (3) [m]
- b exponent of the generator control law (22)
- $\mathbf{b}_{ij}$ input matrix of the radiation R_{ij} [m^{-1}] state-space representation (5)
- $\mathcal{C}$ performance index function (34) [-]
- c_i^* dimensionless quadratic penalty [-] functions (32) and (33)
- $\mathbf{c}_{ij}$ output matrix of the radiation R_{ij} [N] state-space representation (5)
- D outer diameter of the OWC spar-buoy [m]
- d turbine rotor diameter [m]
- F_{di} excitation force on body i (3) [N]
- g acceleration of gravity [m/s^2]
- $\overline{G}_i^*$ time-averaged dimensionless quadratic [-] penalty functions (30)
- $\mathcal{H}$ Hamiltonian function (47)
- $\mathbb{H}$ sum of the Hamiltonian terms that [s^{-1}] depend on u, see (50) and (51)
- I turbine/generator set moment of inertia [kg m^2]
- K_i hydrostatic stiffness of body i [N/m]
- m_i mass of body i [kg]
- p absolute air chamber pressure [Pa]
- p^* dimensionless relative pressure (2) [-]
- p_{at} absolute atmospheric pressure [Pa]
- P_{gen} generator electromagnetic power (22) [W]
- P_{gen}^{rated} generator rated power [W]
- P_{gen}^{ref} ratio of the generator power to the [W] dimensionless generator power (23)
- P_{turb} turbine shaft power (15) [W]
- P_{turb}^* dimensionless turbine shaft power (17) [-]
- P_{turb}^{ref} ratio of the turbine power to the [-] dimensionless turbine power (16)
- Q_{turb} turbine volumetric flow rate [m^3/s]
- R_{ij} radiation damping forces on body i [N] due to body j, see (4) and (5)
- S_1 floater water plane area [m^2]
- S_2 OWC water plane area [m^2]
- t time [s]
- T transpose operator [-]
- T_f time interval of the simulations [s]
- T_{gen} generator electromagnetic torque (24) [N m]
- T_{gen}^{ref} ratio of the generator torque to the [N m] dimensionless generator torque (25)
- T_{RH} receding horizon time interval [s]
- T_{turb} turbine shaft torque (18) [N m]
- T_{turb}^* dimensionless turbine shaft torque (20) [-]
- T_{turb}^{ref} ratio of the turbine torque to the [N m] dimensionless turbine torque (19)
- u status of the HSSV valve (0/1) [-]
- V_0 volume of air inside the chamber [m^3] in calm water
- V_c instantaneous air chamber volume [m^3]
- v_i velocity of body i [m/s]
- w_i constraint i user defined weight [-]
- $\mathbf{x}$ state of system (35)
- $\mathbf{y}_{ij}$ state of the radiation R_{ij} [-] state-space representation (5)
- z_i vertical position body i [m]

Greek symbols
- β constant, (8) [-]
- $\boldsymbol{\lambda}$ adjoint variables
- Δt time interval used to discretize the ODE system (35) [s]
- Δu_n increment of u at time step n, (53) [-]
- η turbine efficiency (14) [-]
- Γ_i excitation force of body i per unit wave amplitude (3) [N/m]
- γ specific heat ratio of air, C_p/C_v [-]
- ω wave frequency (3) [rad/s]
- Ω turbine/generator set rotational speed [rad/s]
- Ω^* dimensionless rotational speed (10) [-]
- Ω_{nom} generator nominal rotational speed [rad/s]
- ν_i constraint i activation constant [-]
- Φ turbine dimensionless mass flow rate (11) [-]
- ϕ_i phase of body i response (3) [rad]
- Π turbine dimensionless power (13) [-]
- Ψ turbine dimensionless pressure head (12) [-]
- ϱ air density [kg/m^3]
- ϱ_{at} air density at atmospheric conditions [kg/m^3]
- ϱ_{ref} reference density assumed $\varrho_{ref} = \varrho_{at}$ [kg/m^3]
- ϱ_w water density [kg/m^3]

Superscripts
- * dimensionless quantity
- bep best efficiency point
- rated rated quantity

Subscripts
- turb turbine quantity
- gen generator quantity
- at atmospheric quantity
- n time step number
- m model scale
- p prototype (full) scale

action alternately compresses and decompresses the trapped air which is forced to flow through a turbine coupled to a generator. The PTO of an OWC device has only one moving part: an air turbine/generator set installed above the water level. The typical turbine rotational speed is in the range of 500–2000 rpm allowing the use of commercial off-the-shelf electrical generators from two-to eight pairs of poles [14]. This configurations reduces the manufacture, installation and maintenance costs.

The safe operation of the PTO system requires the limitation of the pneumatic power available to the turbine. Two valve configurations can be used to control the turbine flow rate: i) a relief valve installed in parallel with the turbine or ii) a HSSV (high-speed stop valve) mounted in series with the turbine. The relief valve is a very appealing concept. However, the large size required for the valve has deterred its application. Apart from PTO protection, the HSSV may have another application: the so-called latching control.

Budal and Falnes in 1977 proposed latching as a way of phase controlling oscillating buoys [15]. This control strategy consists in stopping a WEC during appropriated time intervals in such a

manner that the oscillating velocity is in phase with the excitation force, see Fig. 1. Significant power output gains are achieved if latching is applied in conjunction with optimal control [16,17]. In the presence of regular waves, as in Fig. 1 b), latching control is a mere repetition of the optimal control action for a single period. Latching control under irregular waves is a much more difficult problem, see Fig. 1 c).

Latching control of an OWC device may be performed by opening/closing a HSSV installed in series with the turbine. The first generations of OWC devices used Wells or axial-flow impulse turbines. In this type of turbines, the HSSV must close a large annular duct during a time interval of typically 0.1 s which is a very difficult engineering challenge. Salter [18] proposed a sophisticated pneumatic valve to close the annular duct of the 1.7 m diameter Wells turbine of the Pico plant within the required actuation time. The practical complexity of this type of valves is probably the main reason why, until recently, very few papers were published on OWC latching control [19–23].

An OWC spar-buoy [24] (Fig. 2) and a new type of self-rectifying air turbine, called the biradial turbine [25,26] (Fig. 3), together with latching control, are being developed at Instituto Superior Técnico, Lisbon. The biradial turbine overcomes several limitations of the first generation of self-rectifying air turbines for OWC devices. The turbine is symmetrical with respect to a mid-plane perpendicular to its axis of rotation. The rotor blades are surrounded by a pair of radial-flow guide-vane rows. Each guide vane row is connected to the rotor by an axisymmetric duct whose walls are flat discs. The special geometry of the biradial turbine allows an axially sliding mechanism that operates as a HSSV with a typical stroke of less than 10% of the turbine diameter. Although latching control introduces an increased mechanical complexity in the system, it has been found that an appropriate control of the turbine flow could reduce the overall system costs by decreasing the size of the device for the same extracted power.

In oscillating-body WECs, dynamic forces resulting from latching control must be withstood by the PTO system or by some additional braking system. In most systems, the latching order is only given when the (relative) velocity of the floater with respect to the PTO system is close to zero to reduce dynamic forces and wearing problems. In the case of stiff systems, such as hydraulic circuits or linear generators, this may be seen as a major structural problem especially for dynamic compressive stresses (buckling). System latching under medium to more energetic sea state conditions aggravate these difficulties. Furthermore, the cyclic nature of the wave forces induces major fatigue and wearing problems.

Probably the major problem in what concerns real applications of latching control is the requirement of excitation force prediction over, say, one to three wave periods. Diffraction force prediction over longer than a few wave periods is impossible with the current forecasting state-of-art models. In the present paper, we assume that a prediction horizon of about 10 s–24 s is achievable, possibly

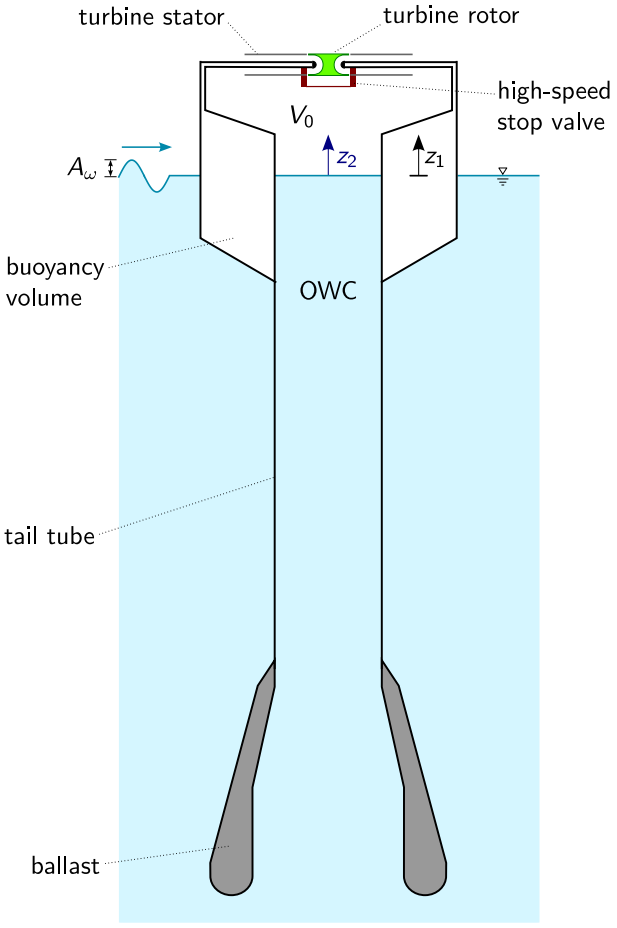

Fig. 2. Longitudinal section of the OWC spar-buoy geometry (not to scale). The device is equipped with a biradial air turbine and a high-speed stop valve in series with the turbine. The high-speed stop valve is shown in the closed position.

with sensors located upwave of the converter. Wave forecasting within this time range has been implemented and tested at the Pico fixed OWC power plant [27,28]. These predictions were based on autoregressive models of the wave elevation inside the OWC chamber and also from upwave elevation measured at a distance of 60 m from the Pico OWC chamber. Although such results were encouraging, it was recognized that they were dependent on the local wave climate and concerned a shoreline OWC plant, not an offshore floating one. Other wave forecasting results based on autoregressive models have been presented in Refs. [29,30]. For the same purpose, Sheng and Lewis used a more computationally demanding strategy based on artificial neural networks [31].

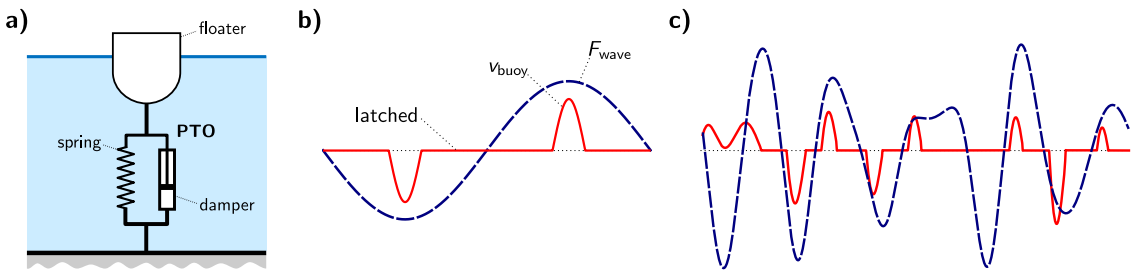

Fig. 1. a) Classical WEC system with a linear PTO reacting against the sea bottom. b) Latching control in regular waves. c) Latching control in irregular sea waves. The velocity of the buoy is v_{buoy}, and F_{waves} is the wave excitation force.

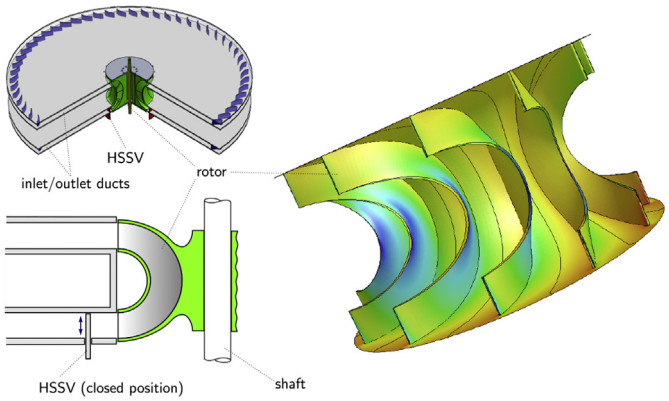

Fig. 3. The biradial turbine and the high-speed stop valve.

The compressibility of the air in the chamber plays an important role in the design and operation of an OWC WEC for several reasons:

- It changes the system response phase.
- From a structural point of view, it reduces the impact forces and fatigue problems, increases the system reliability and, most importantly, decreases structural costs.
- Latching is not expected to be so effective as in the case of an oscillating rigid body WEC, as shown in Fig. 1, since stopping the flow through the turbine does not stop the relative motion between the inner free-surface and the structure.
- It decreases the forces resulting from latching since i) the area of the valve surface subject to the chamber pressure is a small fraction of the area of the OWC free surface and ii) the air compressibility has a spring effect.
- It removes the constraint of latching having to coincide with an instant of zero relative velocity between the floater and the OWC.

The last item is probably the most important to reduce the peak-to-average power ratio. It allows the actuation of the high-speed stop valve whenever required by the control algorithm.

Electrical generators are known to perform poorly at partial loads less than about one third of the rated power. Besides, overheating of the power electronics prevents the rated power from being exceeded. Air turbines behave differently. If their rotational speed is adequately controlled, they are able to work close to the optimum operating point for a very wide range of load conditions.

The focus of the present work is to: i) increase the time averaged turbine power output and ii) to limit the maximum available power to the PTO system by using a control algorithm to open/close a HSSV installed in series with the turbine. This strategy reduces the required rated power of the generator/converter set and increases the power output of the system. The control was implemented within a receding horizon framework [32]. The practical requirements of this type of control were evaluated by simulating and comparing different receding horizon time intervals. The algorithm was tested and validated experimentally in a medium-scale PTO test rig using a hardware-in-the-loop configuration.

In comparison with Refs. [33,34], the new contributions of the present paper are: an improved numerical model of the turbine equipped with a HSSV; a latching control algorithm based on receding horizon strategy with constraints to reduce the turbine peak-to-average power ratio under medium to more energetic sea states; and an enhanced formulation of the scaling laws used for testing the control in a medium-scale PTO test rig.

The paper is organized as follows. The numerical aspects of the overall system are presented in section 2. The optimization problem is introduced in section 3, followed, in section 4, by a short characterization of the test rig where the experimental validation was performed. Numerical results are reported in section 5. Conclusions can be found in section 6.

2. Numerical modelling

2.1. OWC spar-buoy hydrodynamics

Consider the two-body heaving system presented in Fig. 2, where body 1 is the buoy and body 2 is the OWC free surface modelled as rigid piston. The time-dependent coordinates of the heaving bodies 1 and 2 are $z_1(t)$ and $z_2(t)$, respectively, increasing upwards. At equilibrium, $z_1 = z_2 = 0$.

The equations of motion can be found in Ref. [35] for an arbitrary number of oscillating bodies, and in Ref. [36] for the specific case of two bodies oscillating in heave. The equations of motion of bodies 1 and 2, acted upon by sinusoidal waves of frequency ω, are given by

$$\begin{aligned}\left(m_1 + A_{11}^{\infty}\right)\ddot{z}_1 + A_{12}^{\infty}\ddot{z}_2 &= -K_1\, z_1 + S_2\, p_{\mathrm{at}}\, p^* - R_{11} - R_{12} \\ &\quad + F_{d1}, A_{21}^{\infty}\ddot{z}_1 + \left(m_2 + A_{22}^{\infty}\right)\ddot{z}_2 \\ &= -K_2\, z_2 - S_2\, p_{\mathrm{at}}\, p^* - R_{21} - R_{22} + F_{d2}.\end{aligned} \tag{1}$$

Here m_i ($i = 1$ for the floater, $i = 2$ for the OWC) is body mass, A_{ij}^{∞} is the limiting value at infinite frequency of the added mass of body i as affected by the motion of body j, $K_i = \varrho_{\mathrm{w}} g S_i$ is the hydrostatic stiffness of body i where ϱ_{w} is the water density, g is the gravity acceleration, S_1 is the cross sectional area of body 1 defined by the undisturbed free-surface, S_2 is the OWC cross sectional area at the undisturbed free-surface, and p_{at} is the atmospheric pressure. The dimensionless relative pressure is defined as

$$p^* = \frac{p - p_{\mathrm{at}}}{p_{\mathrm{at}}}, \tag{2}$$

where p the absolute air chamber pressure.

The hydrodynamic excitation force on body i is given by

$$F_{di}(\omega_k) = \sum_k \Gamma_i(\omega_k)\, A_{\omega_k} \cos(\,\omega_k\, t + \phi_i(\omega_k)), \tag{3}$$

where k is the number of sinusoidal waves used to discretize a Pierson-Moskowitz spectrum. The amplitude, the excitation force per unit wave amplitude and the phase response of body i as functions of the frequency ω_k of the wave component of order k, are denoted by A_{ω_k}, $\Gamma_i(\omega_k)$ and ϕ_{i_k}, respectively. All the hydrodynamic coefficients of the OWC spar-buoy were computed using a commercial software package [37]. The details about the discretization of the Pierson-Moskowitz spectrum are found in Ref. [33].

The radiation damping forces R_{ij} on body i due to body j are given by

$$R_{ij} = \int_0^t K_{ij}(t-s)\, \dot{z}_j(s)\, \mathrm{d}s. \tag{4}$$

These forces can be represented by the state-space model

$$\dot{\mathbf{y}}_{ij} = \mathbf{A}_{ij}\mathbf{y}_{ij} + \mathbf{b}_{ij}\dot{z}_j, \tag{5}$$

$$R_{ij} = \mathbf{c}_{ij}^T \mathbf{y}_{ij},$$

where $\mathbf{y}_{ij} \in \mathbb{R}^{p\times 1}$, $\mathbf{A}_{ij} \in \mathbb{R}^{p\times p}$, $\mathbf{b}_{ij} \in \mathbb{R}^{p}$, $\mathbf{c}_{ij} \in \mathbb{R}^{p}$, and T denotes the transpose operator. These matrices are obtained using the FDI (Frequency Domain System Identification) toolbox described in Ref. [38]. We use the same degree of approximation p for all the radiation terms.

2.2. Air chamber

Assuming the compression/expansion of the air in the chamber as an isentropic process, the pressure inside the chamber can be related to the volume, V_c, and the flow rate through the turbine, Q_{turb}, by

$$\dot{p}^* = -\gamma(p^*+1)\frac{\dot{V}_c}{V_c} - \gamma(p^*+1)^{\beta}\frac{Q_{turb}}{V_c}, \tag{6}$$

where

$$V_c = V_0 + (z_1 - z_2)S_2, \tag{7}$$

$$\beta = \frac{\gamma-1}{\gamma}, \tag{8}$$

γ is the specific heat ratio for air and V_0 is the volume of air inside the chamber in calm water. In (6) the mass flow rate of air through the turbine is considered to be positive for outward flow, see Ref. [33] for further details. From (6), we found that decreasing the typical air chamber volume, V_c, increases the pressure fluctuations, $\dot{p}^*$, and vice-versa.

2.3. The turbine/generator set

The dynamic of the turbine/generator set is described by

$$\dot{\Omega}^* = \frac{1}{I\Omega_{nom}}(T_{turb} - T_{gen}), \tag{9}$$

where

$$\Omega^* = \frac{\Omega}{\Omega_{nom}} \tag{10}$$

is the dimensionless rotational speed, Ω is the rotational speed, Ω_{nom} is the nominal rotational speed of the generator in radians per unit time, I is the moment of inertia of the turbine/generator set and T_{turb} and T_{gen} are the turbine torque and generator torque. Henceforth, the superscript "*" denotes a dimensionless quantity.

2.3.1. Turbine power and torque

The performance characteristics of a turbine define the relations between the volumetric flow rate, Q_{turb}, the pressure difference, $p - p_{at}$, and the power extracted, P_{turb}, and can be presented in dimensionless form (neglecting the effect of the variations in Reynolds number and Mach number (see [39]) by $\Phi = \Phi(\Psi)$ and $\Pi = \Pi(\Psi)$, where the dimensionless volumetric flow rate, dimensionless pressure head and dimensionless power are

$$\Phi = \frac{Q_{turb}}{\Omega\, d^3}, \tag{11}$$

$$\Psi = \frac{p - p_{at}}{\varrho_{ref}\,\Omega^2\, d^2} = \frac{p^* p_{at}}{\varrho_{ref}\,\Omega^2\, d^2}, \tag{12}$$

$$\Pi = \frac{P_{turb}}{\varrho_{ref}\,\Omega^3\, d^5}, \tag{13}$$

respectively. Here d is the turbine rotor diameter and P_{turb} is the turbine aerodynamic power (equal to the aerodynamic torque times the rotational speed). The reference density ϱ_{ref} is at the turbine inlet stagnation conditions. In the present work we assume the approximation $\varrho_{ref} = \varrho_{at}$.

The turbine efficiency is the ratio between the turbine aerodynamic power and the available pneumatic power

$$\eta = \frac{P_{turb}}{p^*\, p_{at}\, Q_{turb}} = \frac{\Pi}{\Phi\,\Psi}. \tag{14}$$

The turbine flow coefficient Φ, power coefficient Π and efficiency η are plotted in Fig. 4 as functions of the dimensionless pressure head, Ψ. It is remarked that Φ and η are odd and even functions of Ψ.

The turbine aerodynamic power is computed from (14) as

$$P_{turb} = \eta\, p^*\, p_{at}\, Q_{turb} = P_{turb}^{ref}\, P_{turb}^*, \tag{15}$$

where

$$P_{turb}^{ref} = p_{at}\,\Omega_{nom}\, d^3, \tag{16}$$

$$P_{turb}^* = \eta(u\Psi)\, p^*\, \Phi(u\Psi)\,\Omega^*, \tag{17}$$

and u is a control variable that describes the state of the HSSV. The stable operation of the air turbine introduces a severe constraint on the control of the HSSV. Only two HSSV states are allowed: open, $u = 1$, or closed, $u = 0$.

The turbine aerodynamic torque is obtained from (15) as

$$T_{turb} = \frac{1}{\Omega}\,\eta\, p^*\, p_{at}\, Q_{turb} = T_{turb}^{ref}\, T_{turb}^*, \tag{18}$$

where

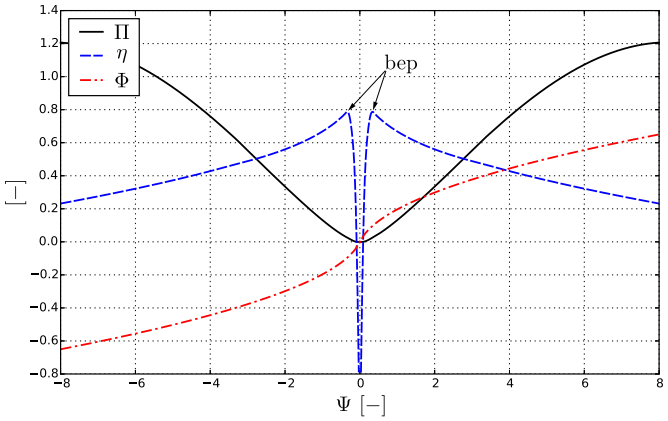

Fig. 4. Efficiency, η, dimensionless mass flow rate, Φ, and dimensionless power, Π, as functions of the dimensionless pressure head, Ψ, of the biradial turbine used in the numerical simulations, adapted from Ref. [26].

$$T^{\text{ref}}_{\text{turb}} = p_{\text{at}}\, d^3, \tag{19}$$

$$T^{*}_{\text{turb}} = \eta(u\Psi)\, p^{*}\, \Phi(u\Psi). \tag{20}$$

2.3.2. Generator power and torque

The turbine best efficiency point, η_{bep}, has a corresponding dimensionless power coefficient Π_{bep}, see Fig. 4. From (13), if only the time-averaged turbine aerodynamic efficiency is to be maximized, then the optimized turbine power is only a power function of the rotational speed

$$P^{\text{bep}}_{\text{turb}} = \varrho_{\text{at}}\, d^5\, \Pi_{\text{bep}}\, \Omega^3. \tag{21}$$

Since, over a long period of time, the net energy stored in the PTO is zero, then, if bearing friction losses are neglected, the time-averaged turbine output power must be equal to the time-averaged generator power $\overline{P}_{\text{turb}} = \overline{P}_{\text{gen}}$. Following [40], the generator power output is modelled using a power law

$$P_{\text{gen}} = a\, \Omega^b = P^{\text{ref}}_{\text{gen}}\, \Omega^{*b}, \tag{22}$$

where

$$P^{\text{ref}}_{\text{gen}} = a\, \Omega^b_{\text{nom}}. \tag{23}$$

The exponent b was found to be slightly greater than 3 to maximize the overall system efficiency (OWC plus turbine), see Fig. 5. The constants a and b are to be determined for the type and geometry of the OWC device and for the characteristics of the air turbine. In the present work, constants a and b were obtained using a least-squares exponential regression of the maximum power output values obtained by an optimization algorithm, as function of the rotational speed, for a given set of sea-states characteristic of the wave climate off the Portuguese Western coast, see Refs. [33,41] for details.

From (22), the generator control law is

$$T_{\text{gen}} = a\, \Omega^{b-1} = T^{\text{ref}}_{\text{gen}}\, \Omega^{*b-1}, \tag{24}$$

where

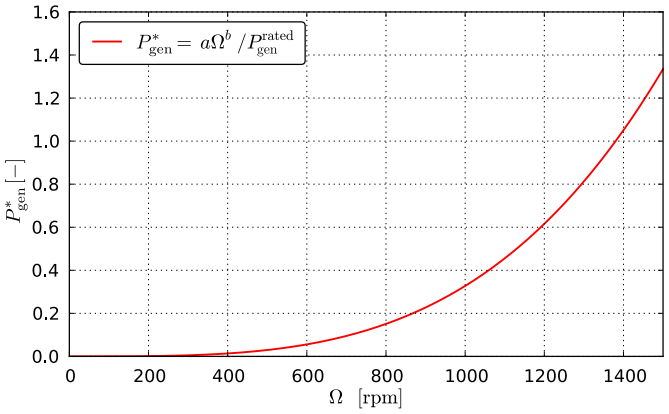

Fig. 5. The basic power-curve control law of the generator, $P^{*}_{\text{gen}} = a\,\Omega^b / P^{\text{rated}}_{\text{gen}}$, obtained from exponential regression of the maximum power extraction computed for a set of sea-states characteristic of the wave climate off the Portuguese west coast. $P^{\text{rated}}_{\text{gen}}$ is the generator rated power.

$$T^{\text{ref}}_{\text{gen}} = a\, \Omega^{b-1}_{\text{nom}}. \tag{25}$$

Using (18) and (24), (9) is finally written as

$$\dot{\Omega}^{*} = \frac{1}{I\,\Omega_{\text{nom}}}\left(T^{\text{ref}}_{\text{turb}}\, T^{*}_{\text{turb}} - T^{\text{ref}}_{\text{gen}}\, \Omega^{*b-1}\right). \tag{26}$$

3. Optimization problem

3.1. The performance index

The aim of the present work is find the control $u(t) \in \{0, 1\}$ that maximizes the dimensionless time-averaged turbine power output along the time interval T_f

$$\overline{P}^{*}_{\text{turb}}\left(\mathbf{x}, u, T_f\right) = \frac{1}{T_f}\int_0^{T_f} P^{*}_{\text{turb}}\, \mathrm{d}t, \tag{27}$$

and, simultaneously, limits the excess of energy available to the turbine

$$P_{\text{turb}} \le \nu_{\text{turb}}\, P^{\text{rated}}_{\text{gen}}, \tag{28}$$

and to the generator

$$P_{\text{gen}} \le \nu_{\text{gen}}\, P^{\text{rated}}_{\text{gen}}, \tag{29}$$

that may occur in medium to more energetic sea states. The symbol $P^{\text{rated}}_{\text{gen}}$ denotes the generator rated power. The control parameters ν_{turb} and ν_{gen} define when the constraint are activated; typically $\nu_{\text{turb}} \gg \nu_{\text{gen}}$.

The constraints are implemented using dimensionless quadratic penalty functions $\overline{G}^{*}_i$ defined as

$$\overline{G}^{*}_i\left(\mathbf{x}, u, T_f\right) = \frac{1}{T_f}\int_0^{T_f} g^{*}_i(\mathbf{x}, u, t)\, \mathrm{d}t, \tag{30}$$

where

$$g^{*}_i(\mathbf{x}, u, t) = -w_i\, u\, c^{*}_i(\mathbf{x}, u, t), \tag{31}$$

and the weights $w_i \ge 0$ are user defined constants.

Using (15) and (22), the dimensionless functions c^{*}_i for the turbine, $i = 1$, and the generator, $i = 2$, are implemented as

$$c^{*}_1(\mathbf{x}, u, t) = \max\left(P^{*}_{\text{turb}} - \nu_{\text{turb}}\, \frac{P^{\text{rated}}_{\text{gen}}}{P^{\text{ref}}_{\text{turb}}}, 0\right)^2, \tag{32}$$

$$c^{*}_2(\mathbf{x}, u, t) = \max\left(\Omega^{*b} - \nu_{\text{gen}}\, \frac{P^{\text{rated}}_{\text{gen}}}{P^{\text{ref}}_{\text{gen}}}, 0\right)^2. \tag{33}$$

The first constraint $\overline{G}^{*}_1$ is a non-linear function of u.

For the control strategy, we want to determine $u(t)$ that maximizes the performance index

$$\mathcal{C}\left(\mathbf{x}, u, T_f\right) = \overline{P}^{*}_{\text{turb}}\left(\mathbf{x}, u, T_f\right) + \overline{G}^{*}_1\left(\mathbf{x}, u, T_f\right) + \overline{G}^{*}_2\left(\mathbf{x}, u, T_f\right), \tag{34}$$

subjected to the constraint $u \in \{0,1\}$, for $0 \le t \le T_f$.

3.2. The numerical model as a first-order system of ODEs

The system of Eqs. (1), (6) and (27) and constraints (30) can be written as a system of first-order ODEs (ordinary differential equations) in vectorial form

$$\dot{\mathbf{x}} = \mathbf{F}(\mathbf{x}, \mathbf{u}), \tag{35}$$

where

$$\mathbf{x} = \begin{pmatrix} v_1 & v_2 & z_1 & z_2 & p^* & \Omega^* & \overline{P}^*_{\text{turb}} & \overline{G}^*_1 & \overline{G}^*_2 & \mathbf{y}_{11}^T & \mathbf{y}_{12}^T & \mathbf{y}_{21}^T & \mathbf{y}_{22}^T \end{pmatrix}^T. \tag{36}$$

Using (36), the right-hand side of (35) becomes

$$\mathbf{F}(\mathbf{x},u) = \begin{pmatrix} F_1 \\ F_2 \\ F_3 \\ F_4 \\ F_5 \\ F_6 \\ F_7 \\ F_8 \\ F_9 \\ \mathbf{F}_{11} \\ \mathbf{F}_{12} \\ \mathbf{F}_{21} \\ \mathbf{F}_{22} \end{pmatrix} = \begin{pmatrix} M_2^* \mathcal{F}_1 - A_{12}^* \mathcal{F}_2 \\ M_1^* \mathcal{F}_2 - A_{21}^* \mathcal{F}_1 \\ v_1 \\ v_2 \\ -\gamma(p^*+1)\dfrac{\dot{V}_c}{V_c} - \gamma(p^*+1)^{\beta}\dfrac{Q_{\text{turb}}}{V_c} \\ \dfrac{1}{I\,\Omega_{\text{nom}}}\left(T^{\text{ref}}_{\text{turb}}\, T^*_{\text{turb}} - T^{\text{ref}}_{\text{gen}}\, \Omega^{*b-1}\right) \\ P^*_{\text{turb}}\, T_f^{-1} \\ g_1^*\, T_f^{-1} \\ g_2^*\, T_f^{-1} \\ \mathbf{A}_{11}\mathbf{y}_{11} + \mathbf{b}_{11} v_1 \\ \mathbf{A}_{12}\mathbf{y}_{12} + \mathbf{b}_{12} v_2 \\ \mathbf{A}_{21}\mathbf{y}_{21} + \mathbf{b}_{21} v_1 \\ \mathbf{A}_{22}\mathbf{y}_{22} + \mathbf{b}_{22} v_2 \end{pmatrix}, \tag{37}$$

where

$$\dot{z}_1 = v_1, \tag{38}$$

$$\dot{z}_2 = v_2, \tag{39}$$

$$\mathcal{D} = \left(M_1 M_2 - A_{12}^{\infty} A_{21}^{\infty}\right)^{-1}, \tag{40}$$

$$M_i^* = \mathcal{D}\left(m_i + A_{ii}^{\infty}\right), \tag{41}$$

$$A_{ij}^* = \mathcal{D} A_{ij}^{\infty}, \tag{42}$$

$$\begin{aligned} \mathcal{F}_1 &= -K_1\, z_1 + S_2\, p_{\text{at}}\, p^* + F_{d1} - \mathbf{c}_{11}^T \mathbf{y}_{11} - \mathbf{c}_{12}^T \mathbf{y}_{12} \\ &= -K_1\, z_1 + S_2\, p_{\text{at}}\, p^* + F_{d1} - \mathbf{c}_{11}^T \mathbf{y}_{11} - \mathbf{c}_{12}^T \mathbf{y}_{12}, \end{aligned} \tag{43}$$

$$\begin{aligned} \mathcal{F}_2 &= -K_2\, z_2 - S_2\, p_{\text{at}}\, p^* + F_{d2} - \mathbf{c}_{21}^T \mathbf{y}_{21} - \mathbf{c}_{22}^T \mathbf{y}_{22} \\ &= -K_2\, z_2 - S_2\, p_{\text{at}}\, p^* + F_{d2} - \mathbf{c}_{21}^T \mathbf{y}_{21} - \mathbf{c}_{22}^T \mathbf{y}_{22}. \end{aligned} \tag{44}$$

Hereafter, we will assume that vectors are column vectors, and block notation in vectors and matrices will be used.

The initial condition of the state $\mathbf{x}$ in (35) is

$$\mathbf{x}_0 = \begin{pmatrix} 0 & 0 & 0 & 0 & 0 & \Omega_0^* & 0 & 0 & 0 & 0_n^T & 0_n^T & 0_n^T & 0_n^T \end{pmatrix}^T, \tag{45}$$

where 0_p denotes a zeros column vector with dimension p.

3.3. The Pontriagyn Maximum Principle

The optimal control problem consists in computing the instantaneous state of the HSSV, $u(t)$, that maximizes the performance index associated with the final state $\mathcal{C}(T_f)$ given by (34).

Following the PMP (Pontriagyn Maximum Principle), let us define the functional [42].

$$\mathcal{J}(u) = \mathcal{C}\left(T_f, \mathbf{x}, u\right) - \int_0^{T_f} \boldsymbol{\lambda}^T (\dot{\mathbf{x}} - \mathbf{F}(\mathbf{x}, u))\, \mathrm{d}t. \tag{46}$$

The components of vector $\boldsymbol{\lambda}$, named co-states, can be viewed as Lagrange multipliers used to compute the optimal solution $u(t)$ subjected to satisfy the system of (35). The PMP states that, at each instant t, the Hamiltonian

$$\mathcal{H}(\mathbf{x}, u, \boldsymbol{\lambda}) = \boldsymbol{\lambda}^T\, \mathbf{F}(\mathbf{x}, u), \tag{47}$$

is maximum for the optimal input u. Along the optimal control path $(\mathbf{x},\boldsymbol{\lambda},u)$, the co-states are computed from

$$\dot{\boldsymbol{\lambda}} = -\nabla_{\mathbf{x}} \mathbf{F}(\mathbf{x}, u)^T\, \boldsymbol{\lambda}, \tag{48}$$

subjected to the terminal condition

$$\boldsymbol{\lambda}\left(T_f\right) = \nabla_{\mathbf{x}}\, \mathcal{C}\left(T_f\right)^T. \tag{49}$$

Eq. (48) is the so-called adjoint equation. Eq. (46) reveals that we need to have a wave prediction over the time interval of the optimal control problem, T_f.

Considering the structure of the adjoint system of equations, it is concluded that $\lambda_7 = \lambda_8 = \lambda_9 = 1$. Using these values for the adjoint variables and denoting by $\mathbb{H}$ the terms of the Hamiltonian H that depend on u, we get

$$\begin{aligned} \mathbb{H}(\mathbf{x}, u, \boldsymbol{\lambda}) = &-\lambda_5\, \gamma(p^*+1)^{\beta}\frac{Q_{\text{turb}}}{V_c} + \lambda_6\, \frac{1}{I\Omega_{\text{nom}}}\, T^{\text{ref}}_{\text{turb}}\, T^*_{\text{turb}} \\ &+ \frac{1}{T_f}\left(P^*_{\text{turb}} + g_1^* + g_2^*\right). \end{aligned} \tag{50}$$

For the present analysis it is convenient to write (50) as

$$\begin{aligned} \mathbb{H}(\mathbf{x}, u, \boldsymbol{\lambda}) = &-\lambda_5\, \gamma(p^*+1)^{\beta}\frac{\Omega\, d^3}{V_c}\, \Phi(u\,\Psi) + \frac{\rho_{\text{at}}\, \Omega^2\, d^2}{\Omega_{\text{nom}}}\left(\frac{\lambda_6\, d^3}{I}\right. \\ &\left. + \frac{\Omega}{T_f\, p_{\text{at}}}\right)\Pi(u\,\Psi) \\ &- \frac{w_1\, u}{T_f}\, \max\left(\frac{\rho_{\text{at}}\, \Omega^3\, d^5}{P_{\text{ref}}}\, \Pi(u\,\Psi) - \nu_{\text{turb}}\, \frac{P^{\text{rated}}_{\text{gen}}}{P^{\text{ref}}_{\text{turb}}}, 0\right)^2 \\ &- \frac{w_2\, u}{T_f}\, \max\left(\Omega^{*b} - \nu_{\text{gen}}\, \frac{P^{\text{rated}}_{\text{gen}}}{P^{\text{ref}}_{\text{gen}}}, 0\right)^2. \end{aligned} \tag{51}$$

Eq. (51) is a non-linear function of the control variable u, and the optimal HSSV command is computed as follows.

The stable operation of the air turbine implies a two-position HSSV: close or opened. The optimal HSSV command is such that it maximizes $\mathbb{H}(\mathbf{x}, u, \boldsymbol{\lambda})$ constrained to $u \in \{0, 1\}$. Therefore, we get a bang–bang type of control. From (51), it is possible to check that, if the HSSV is closed, $u = 0$, then $\mathbb{H}(\mathbf{x}, u, \boldsymbol{\lambda}) = 0$, since $\Phi(0) = \Pi(0) = 0$, see Fig. 4. Moreover, $\mathbb{H}$ is maximized if $\mathbb{H}(\mathbf{x}, u, \boldsymbol{\lambda}) > 0$ when the HSSV is opened, $u = 1$.

The optimal HSSV command is computed using the switching function

$$u(t) = \begin{cases} 1, & \text{if } \mathbb{H}(\mathbf{x}, u, \boldsymbol{\lambda}) > 0 \text{ when } u = 1, \\ 0, & \text{otherwise.} \end{cases} \tag{52}$$

The current optimal problem has no singular arcs. The only condition for which $\mathbb{H}(\mathbf{x}, u, \boldsymbol{\lambda})$ is independent of the value of u is when $p^* = 0$ and all the constraints are not active, $g_i^* = 0$. For the wave spectra studied, this condition only occurs in the instants where p^* changes the sign.

The most important detail in the implementation of the constraints is the multiplication of $c_i^*(\mathbf{x}, u, t)$ by the control variable u, see (30) and (31). This introduces the constraints g_i^* in the Hamiltonian terms that depend on u, $\mathbb{H}(\mathbf{x}, u, \boldsymbol{\lambda})$.

3.4. Receding horizon latching control

A wave prediction time interval that corresponds to an optimization interval, T_f, of seral minutes is not possible to achieve with the current sea waves forecasting models. To implement a realizable latching control in real-time we need a fast algorithm capable of computing a sub-optimal solution using a short prediction time interval. In the present work, a receding horizon approach was adopted [32,43].

Hereafter, we will assume a discrete non-linear solution for the control problem with a time-step Δt. We define $\mathbf{x}_n = \mathbf{x}(t_n)$, $u_n = u(t_n)$, $t_n = n\,\Delta t$, $T_f = M\,\Delta t$, where M and n are integers such that $n = 0,\ldots,M$.

Let us consider a constant short-term-prediction time interval, T_{RH}, that starts at the current instant t_n, such that $T_{\text{RH}} = m\,\Delta t$, see Fig. 6. We compute the position of the latching valve for the next time interval, u_{n+1}, based on PMP considering the wave prediction within the time interval T_{RH}. As time advances to the next time step, t_{n+1}, we update the wave prediction over the time interval, T_{RH}, shifted forward (hence the name moving or receding horizon control) and compute the position of the latching valve for the next time interval, u_{n+2}. To improve the computational efficiency of the algorithm, we use the previous control solution, u_i, computed in the previous time step within the receding horizon, $i = n + 1,\ldots,n + m$, as the initial condition of the present computations, see arrows in Fig. 6.

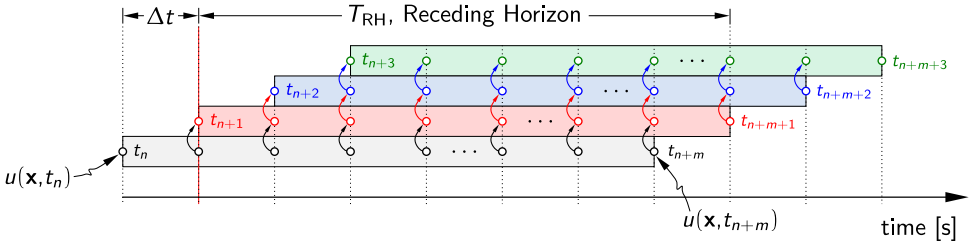

Fig. 6. Receding horizon control.

Algorithm 1 Receding horizon real-time control

for i such that $i = 1, \ldots, M + m$ **do**
  $u_i \leftarrow 1$
end for
set the initial conditions at instant t_1: $\mathbf{x}_1$ and u_1
for n such that $n = 1, \ldots, M$ **do**
  apply the command u_n to the high-speed stop valve
  read the experimental value of Ω_n and use it as an initial condition
  compute the final condition at instant t_{n+m}: $\boldsymbol{\lambda}_{n+m}$
  forward solve $\dot{\mathbf{x}} = \mathbf{F}(\mathbf{x}, u)$, for $\mathbf{x}_i$ such that $i = n, \ldots, n + m$
  backward solve $\dot{\boldsymbol{\lambda}} = -\nabla_{\mathbf{x}}\mathbf{F}(\mathbf{x}, u)^{\mathsf{T}}\,\boldsymbol{\lambda}$, for $\boldsymbol{\lambda}_i$ such that $i = n + m, \ldots, n$
  for i such that $i = n + m, \ldots, n$ **do**
    $\Delta u_i = G\,\text{sign}(\,\mathbb{H}(\mathbf{x}_i, \boldsymbol{\lambda}_i, u = 1)\,)$
    $u_i = \text{round}(\,\max(\,\min(\,u_i + \Delta u_i,\, 1\,),\, 0\,)\,)$
  end for
end for

An iterative algorithm is adopted to compute the control u_i. From the numerical point-of-view, this algorithm may be viewed as a successive under-relaxation method. Let us start by computing an update to the control variable u_n based on $\mathbb{H}$ when $u = 1$,

$$\Delta u_n = G\ \mathrm{sign}(\ \mathbb{H}(\mathbf{x}_n, \boldsymbol{\lambda}_n, u = 1)\ ), \tag{53}$$

where

$$\mathrm{sign}(x) = \begin{cases} -1, & x < 0\,, \\ 0, & x = 0\,, \\ +1, & x > 0\,, \end{cases} \tag{54}$$

and G is a user-defined gain. The control variable is updated in each iteration by

$$u_n = \mathrm{round}(\ \max(\ \min(\ u_n + \Delta u_n,\ 1\ ),\ 0\ )\ )\,, \tag{55}$$

where

$$\mathrm{round}(x) = \begin{cases} 0, & x < 0.5\,, \\ 1, & x \geq 0.5\,. \end{cases} \tag{56}$$

The adopted procedure is described in Algorithm 1.

Stability problems were found in the numerical solution of the adjoint (48). This behaviour is reported in Bryson and Ho [44]. The aim of using the dimensionless variables p^*, Ω^*, $\overline{P}^*$, $\overline{G}_1^*$ and $\overline{G}_2^*$ is to improve the convergence properties of the ODE system (48) by having the same order of magnitude for all the variables, $\mathcal{O}[\mathbf{x}] = 1$. For the present control problem, the 5th-order Dormand-Prince method was the lowest order ODE solver that was able to obtain a stable solution of the adjoint equation. This method was also used to solve (35), thus ensuring the same order of accuracy in the overall solution of the control problem.

4. The Tecnalia PTO test rig

4.1. Experimental setup

The Tecnalia test rig is represented schematically in Fig. 7. The objective of the tests is to evaluate the generator dynamics by simulating the turbine via a motor where its supplied torque is computed in real-time as a function of the instantaneous sea state conditions.

The motor and the generator are coupled through a shaft where a flywheel is mounted to increase the inertia. The motor is a two-pair-of-poles squirrel cage induction motor with a rated power of 15 kW. The nominal and the maximum rotational speeds are 1460 rpm and 1800 rpm, respectively. The motor is controlled by a frequency converter with a rated power of 18 kW. It allows power-peaks up to 28 kW. The generator is a squirrel cage induction generator with a rated power of 11 kW. The nominal and the maximum rotational speeds are 768 rpm and 1000 rpm, respectively. The generator is connected to an isolated grid with 400 V through a back-to-back power converter. The power converter rated power is 11 kW and controls the generator electromagnetic torque using an analogue signal supplied by the computer. A PLC (programmable-logic-controller) controls the system start-up and shut-down, and monitors any failure.

The test rig losses were found to be nearly proportional to the rotational speed, $P_{\mathrm{loss}} = T_{\mathrm{loss}}\,\Omega$, the associated torque being equal to $T_{\mathrm{loss}} = 3.08$ Nm within the safe operation limits. A constant compensation torque is added to the motor to cancel the losses, T_{loss}. At each time-step, the measured instantaneous rotational speed is used as initial condition, Ω_0, of Algorithm 2, see (45) and Fig. 7. The rotational speed is measured directly in the computer using the signal of the encoder attached to the motor shaft. Further details about the test rig can be found in Ref. [33].

4.2. Scaling laws

In the test bench we have the problem of how to respect the dynamic similitude if we are not able to scale the inertia and the rotational speed according to Froude's scaling law.

The equations for modelling the rotational speed of a turbine/generator set at prototype (full) scale (subscript p) are

$$I_p\ \frac{\mathrm{d}\Omega_p}{\mathrm{d}t} = T_{\mathrm{turb}_p} - T_{\mathrm{gen}_p}\,. \tag{57}$$

Using Froude's scaling criterion, the inertia, rotational speed and torque of the model (subscript m) are given by

$$I_m = \left(\frac{D_m}{D_p}\right)^5 I_p, \tag{58}$$

$$\Omega_m = \left(\frac{D_p}{D_m}\right)^{\frac{1}{2}} \Omega_p, \tag{59}$$

$$T_m = \left(\frac{D_m}{D_p}\right)^4 T_p, \tag{60}$$

yielding

$$I_m \frac{\mathrm{d}\Omega_m}{\mathrm{d}t} = T_{\mathrm{turb}_m} - T_{\mathrm{gen}_m}\,. \tag{61}$$

However, the maximum rotational speed that can be used in the test bench is much lower than the model rotational speed, Ω_m. To

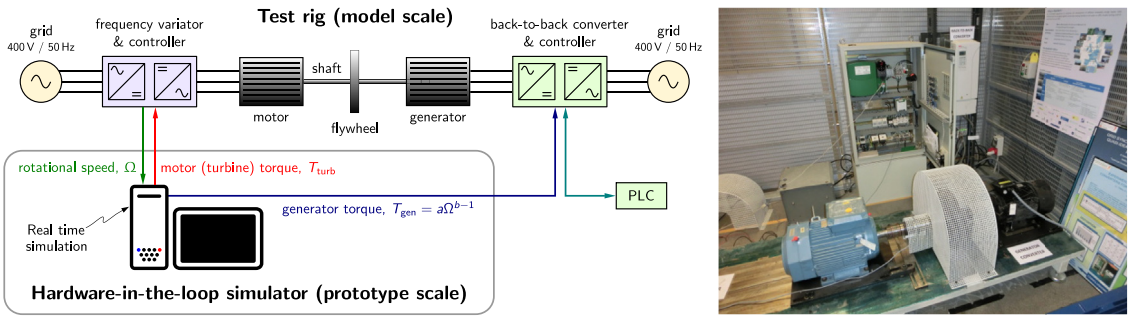

Fig. 7. Configuration used for the hardware-in-the-loop validation tests.

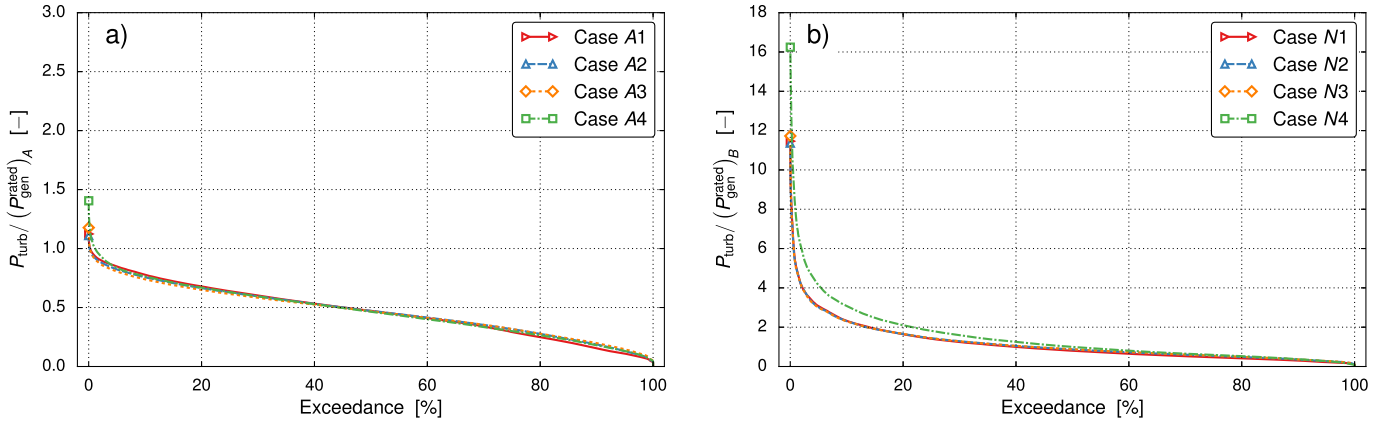

Fig. 8. Generator power exceedance curves for: a) set A and b) set N. Note that the upper limit of ordinates in Fig. 8 b) is 6 times the upper limit in Fig. 8 a).

scale the rotational speed while obeying the dynamic similitude we proceed as follows. Let us define a rotational speed, Ω_r, related to the model rotational speed by

$$\Omega_r = \kappa\, \Omega_m. \tag{62}$$

where $0 < \kappa < 1$. Hereafter, the subscript r denotes a test bench quantity. Taking the time derivative of (62) and substituting in (61) we get, after rearranging,

$$\frac{\mathrm{d}\Omega_r}{\mathrm{d}t} = \frac{\kappa}{I_m}\left(T_{\text{turb}_m} - T_{\text{gen}_m}\right). \tag{63}$$

The inertia of the test bench rotating parts is I_r. If we multiply both sides of (63) by the test bench inertia we get

$$I_r \frac{\mathrm{d}\Omega_r}{\mathrm{d}t} = \kappa \frac{I_r}{I_m}\left(T_{\text{turb}_m} - T_{\text{gen}_m}\right) = T_{t_r} - T_{g_r} \tag{64}$$

where

$$T_{t_r} = \kappa \frac{I_r}{I_m}\, T_{\text{turb}_m} = \kappa \frac{I_r}{I_m}\left(\frac{D_m}{D_p}\right)^4 T_{\text{turb}_p} = \kappa \frac{I_r}{I_p}\,\frac{D_p}{D_m}\, T_{\text{turb}_p}, \tag{65}$$

and

$$T_{g_r} = \kappa \frac{I_r}{I_m}\, T_{\text{gen}_m} = \kappa \frac{I_r}{I_m}\left(\frac{D_m}{D_p}\right)^4 T_{\text{gen}_p} = \kappa \frac{I_r}{I_p}\,\frac{D_p}{D_m}\, T_{\text{gen}_p}. \tag{66}$$

Eq. (64) represents the dynamics of the test bench. In order to respect the angular acceleration of the model, that is related to the test bench angular acceleration through (62), we need to compensate the torque of the model by a factor equal to $(\kappa\, I_r/I_m)$.

Denoting by D the OWC spar-buoy outer diameter, the scale of the tests, D_m/D_p, is determined as function of the ratio between the rated powers of the generator of the test bench, P_{g_r} and the generator of the prototype, P_{g_p},

$$\frac{D_m}{D_p} = \left(\frac{P_{g_r}^{\text{rated}}}{P_{g_p}^{\text{rated}}}\right)^{\frac{2}{7}}. \tag{67}$$

The velocity ratio κ can be computed from the ratio of the nominal speed of test bench and nominal speed that should be used at model scale

$$\kappa = \frac{\Omega_{\text{nom},r}}{\Omega_{\text{nom},m}}, \tag{68}$$

where $\Omega_{\text{nom},m}$ is computed from the prototype scale using (59),

$$\Omega_{\text{nom},m} = \Omega_{\text{nom},p}\left(\frac{D_p}{D_m}\right)^{\frac{1}{2}}. \tag{69}$$

Assuming a relation between Ω_r and Ω_m as given by (68), we find, from (62) and using (68), (69) and (59), a simple relation between the rotational speeds of the test bench and the prototype

$$\Omega_r = \frac{\Omega_{\text{nom},r}}{\Omega_{\text{nom},p}}\, \Omega_p. \tag{70}$$

5. Results

The OWC spar buoy diameter used in the computations was $D_p = 12$ m. Only irregular sea states were considered in the presented tests. The sea states were described by a Pierson-Moskowitz variance density spectrum [45] with a 6 m significant wave height. These are rather highly energetic sea states since the objective was to test the limits of the control algorithm.

The duration of each test and the time step at prototype scale were 2400 s and 0.1 s, respectively. The radiation terms R_{ij} were computed with a 5th order state-space approximation, $p = 5$. The resulting system of ODEs, (35), comprises 29 equations. Since the system does not store energy over a long time interval, the time average turbine power output equals the time averaged generator power output, $\overline{P}_{\text{gen}} = \overline{P}_{\text{turb}}$. Hereafter, to allow a better assessment of the performance of the control algorithm, the turbine output power is presented in dimensionless form by dividing by the generator rated power, $P_{\text{gen}}^{\text{rated}}$, which is assumed to be constant for each set tests. Table 1 summarizes the results discussed in the present paper.

The set of tests A uses the generator with the highest rated power, see Table 1. Sets A and N allow the comparison of the results between constrained and unconstrained control for the same conditions. The results of set N were obtained without hardware-in-the-loop, scale being thereby meaningless in this configuration. Both sets show the effect of the receding horizon time interval in the system performance for a turbine/generator set with low inertia. The time-averaged turbine power output, $\overline{P}_{\text{turb}}/(P_{\text{gen}}^{\text{rated}})_{\text{A}}$, is almost constant for the receding horizons of $T_{\text{RH}} = \{2, 4, 8\}$ s, cases A1 through A3. The same behaviour is found for cases N1 through N3. The comparison of cases A1 through A3 with cases N1 through

Table 1
Summary of the tests. HIL stands for hardware-in-the-loop configuration. Set N presents results for unconstrained control.

Fig	HIL	Set	Case	Sea state		Inertia I_p [kg m^2]	R. Horiz T_{RH} [s]	Test scale [−]	$\frac{P_{gen}^{rated}}{(P_{gen}^{rated})_A}$ [%]	$\frac{\overline{P}_{turb}}{P_{gen}^{rated}}$ [%]	$\frac{\overline{P}_{turb}}{(P_{gen}^{rated})_A}$ [%]	Coeff. υ_{turb} [−]
				T_e [s]	H_s [m]							
8 a)	Yes	A	A1	8	6	200	2	3.135	100	41.6	41.6	3
			A2	8	6	200	4	3.135	100	41.6	41.6	3
			A3	8	6	200	8	3.135	100	41.3	41.3	3
			A4	8	6	200	16	3.135	100	44.1	44.1	3
8 b)	No	N	N1	8	6	200	2	–	100	57.8	57.8	3
			N2	8	6	200	4	–	100	58.4	58.4	3
			N3	8	6	200	8	–	100	58.6	58.6	3
			N4	8	6	200	16	–	100	73.4	73.4	3
9 a)	Yes	B	B1	8	6	200	2	2.572	50	72.5	36.3	6
			B2	8	6	200	4	2.572	50	67.1	33.5	6
			B3/C1	8	6	200	8	2.572	50	61.7	30.8	6
			B4	8	6	200	16	2.572	50	56.8	28.4	6
9 b)	Yes	C	C1/B3	8	6	200	8	2.572	50	61.7	30.8	6
			C2	10	6	200	8	2.572	50	60.9	30.4	6
			C3	12	6	200	8	2.572	50	53.4	26.7	6
			C4	16	6	200	8	2.572	50	25.8	12.9	6
10	Yes	D	D1	8	6	600	8	2.572	50	68.2	34.1	8
			D2	10	6	600	8	2.572	50	62.2	31.1	6
			D3	12	6	600	8	2.572	50	55.0	27.5	6
			D4	16	6	600	8	2.572	50	23.6	11.8	6

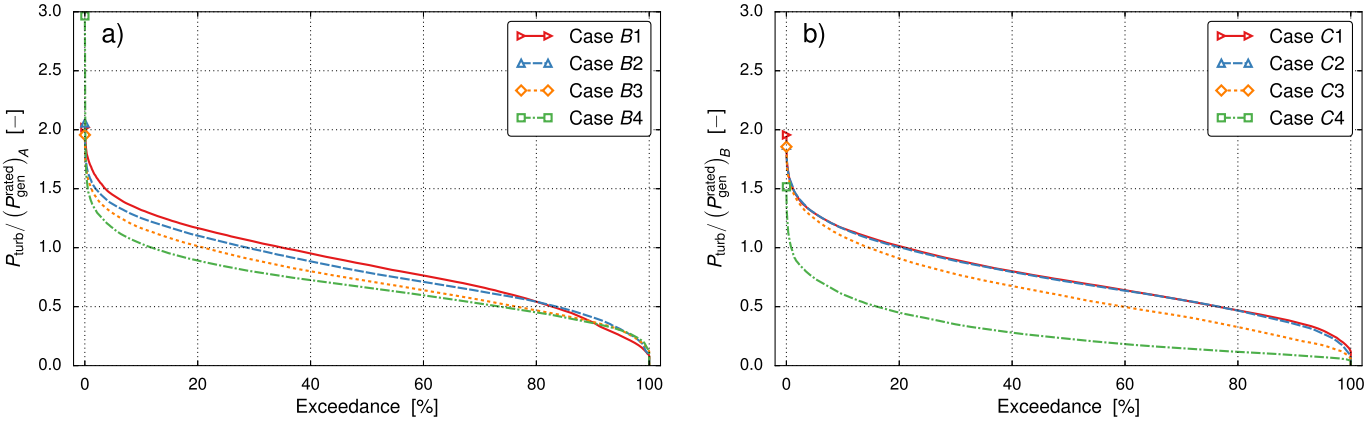

Fig. 9. Generator power exceedance curves for: a) set B and b) set C.

N3, shows that the constraints impose a large reduction in the time average turbine output power. Comparing case A4, $T_{RH} = 16$ s, with cases A1 through A3, we find that the receding horizon increase does not improve significantly the time average turbine power output due to the constraints. This conclusion is evidenced by comparing the case N4 with cases N1 to N3. The unconstrained control is particularly effective for the receding horizon interval of $T_{RH} = 16$ s, case N4.

The instantaneous turbine power output exceedance curves for sets A and N are plotted in Fig. 9. In set A, the constraints are violated only 1% of the time, $P_{gen}/P_{gen}^{rated} > 1$. For the case N1, the generator rated power is exceeded 40% of the time, and in case N4 this value increases to 50%. Comparing the power peaks for sets A and N, the constrained control reduces these peaks by one order of magnitude, in comparison with unconstrained control.

The generator rated power for sets B and C is half of the generator rated power of set A,

$$\left(P_{gen}^{rated}\right)_{\{B,C\}} = \frac{1}{2}\left(P_{gen}^{rated}\right)_A. \tag{71}$$

Table 1 shows that set B has a much higher generator load than set A,

$$\left(\frac{\overline{P}_{turb}}{P_{gen}^{rated}}\right)_B > \left(\frac{\overline{P}_{turb}}{P_{gen}^{rated}}\right)_A. \tag{72}$$

The reduction in the generator rated power increases the number of time intervals where the constraint g_2^* is active. In set B, the time-averaged turbine output power decreases with the increase in the receding horizon time interval. This behaviour results from a better handling of the constraint g_2^* by the control with the increase of the receding horizon.

Set C shows the influence of the period of energy of the spectrum in the time-averaged generator output. As expected in this case, the performance of the system decreases with the increase in the energy period.

Comparing Fig. 9 a), we find that the generator working load is higher in set B than in set A, as the area below comparable curves is higher for the cases of set N. However, the peak power is much larger in set B than in set A.

From the analysis of the results obtained for set B, it is clear that the proposed control algorithm is unable to handle highly energetic sea states without violating the constraint g_2^*. This behaviour can be understood through (51) and (52). During the tests and for short time intervals, the co-states λ_5 and λ_6 take large values and the

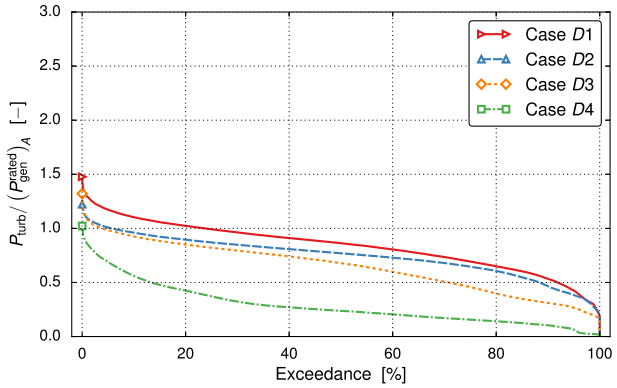

Fig. 10. Generator power exceedance curves for set D.

Hamiltonian, (50), is positive although the constraints are active and have a negative contribution. This is a consequence of introducing the constraints via a quadratic penalty function in the numerical method.

The simplest method to avoid the generator overpower is to saturate the instantaneous generator power at the rated power, thus relaxing the rotational speed control of the generator. However, this approach was not adopted to fully understand the limits of the proposed method. An alternative approach to address the constraint violation is to close the high-speed stop valve using an outer control loop. However, this option was also discarded. Nevertheless, important conclusions can be drawn from the results.

Finally, the last set of tests D shows the effect of increasing the inertia of the rotating parts of the turbine/generator set. The inertia ratio between sets D and C is $I_D/I_C = 3.0$. For constrained control, the effect of increasing the inertia in a system with low generator rated power is to increase the averaged turbine power output, see Fig. 10. As a result of the larger inertia, the constraints are active for shorter time periods due to the smaller amplitudes of the instantaneous turbine power output. The comparison of exceedance curves for sets C and D showed no significant differences apart from the lower power peaks for set D.

6. Conclusions

A constrained latching control algorithm for an OWC floating WEC was implemented and tested in a large scale test rig connected to the power grid. The simplicity of the biradial turbine equipped with a sliding high-speed stop valve opened the possibility of controlling the excess of energy available to the turbine/generator set. The compressibility of the air allows the operation of the high-speed stop valve whenever required by the control algorithm, which is not possible for stiff systems like hydraulic PTOs or linear direct drive electrical generators. This is a great advantage of OWC based devices.

The biradial air turbine has the ability to operate around the best efficiency point for a wide range of loading conditions and system's inertia. Unconstrained control with a low inertia system extracts more energy due to the faster response of the turbine/generator set to the available pneumatic power peaks. In the case of a system with low generator rated power, constrained control extracts more energy in a system with a higher inertia. The higher inertia decreases the power peaks thus reducing the time periods during which the constraints imposed by the control algorithm force the high-speed stop valve to remain closed.

The proposed constrained control was found to be able to increase the generator load and to greatly reduce the output power peaks of the turbine with a relatively small decrease in the time-averaged turbine power output. The presented results also show that, within certain limits, a reduction in the generator rated power increases the generator mean load at the expense of an only slight decrease in the time-averaged turbine power output.

The major drawback of the proposed control algorithm is the violation of the constraints under certain conditions during very short time periods. This is a consequence of imposing the constraints with quadratic penalty functions. Future work will be devoted to devise an alternative control algorithm based on the method of indirect adjoints with state inequality constraints.

Acknowledgements

The research was partially funded by the European Community's Seventh Framework Programme under MARINET (Marine Renewables Infrastructure Network) initiative, grant agreement No. 262552. This work was also funded by the Portuguese Foundation for Science and Technology (FCT) through IDMEC, under LAETA Pest-OE/EME/LA0022, and by the European Union's Horizon 2020 program, project WETFEET, under grant No. 646436. The first author was supported by FCT researcher grant No. IF/01457/2014. The third author was supported by FCT through INESC-ID under UID/CEC/50021/2013. The fourth author was supported by post-doctoral fellowship SFRH/BPD/93209/2013 from FCT.

References

[1] Lund H. The kyoto mechanisms and technological innovation. Energy 2006;31(13):2325–32. http://dx.doi.org/10.1016/j.energy.2006.01.010.
[2] Graça Carvalho M da. EU energy and climate change strategy. Energy 2012;40(1):19–22. http://dx.doi.org/10.1016/j.energy.2012.01.012.
[3] Umbach F. Global energy security and the implications for the EU. Energy Policy 2010;38(3):1229–40. http://dx.doi.org/10.1016/j.enpol.2009.01.010.
[4] Lund H. Renewable energy strategies for sustainable development. Energy 2007;32(6):912–9. http://dx.doi.org/10.1016/j.energy.2006.10.017. third Dubrovnik Conference on Sustainable Development of Energy, Water and Environment Systems.
[5] Lund H, Mathiesen B. Energy system analysis of 100% renewable energy systems – the case of Denmark in years 2030 and 2050. Energy 2009;34(5):524–31. http://dx.doi.org/10.1016/j.energy.2008.04.003. 4th Dubrovnik Conference4th Dubrovnik conference on Sustainable Development of energy, Water & Environment.
[6] Lund H, Østergaard PA, Stadler I. Towards 100% renewable energy systems. Appl Energy 2011;88(2):419–21. http://dx.doi.org/10.1016/j.apenergy.2010.10.013.
[7] de AF, Falcão O. Wave energy utilization: a review of the technologies. Renew Sustain Energy Rev 2010;14(3):899–918. http://dx.doi.org/10.1016/j.rser.2009.11.003.
[8] R. Bucher, I. Bryden, Overcoming the marine energy pre-profit phase: what classifies the game-changing "array-scale success"?, Int J Mar Energy, http://dx.doi.org/10.1016/j.ijome.2015.05.002 (in press).
[9] Magagna D, Uihlein A. Ocean energy development in europe: current status and future perspectives. Int J Mar Energy 2015;11:84–104. http://dx.doi.org/10.1016/j.ijome.2015.05.001.
[10] Ferguson TM, Fleming A, Penesis I, Macfarlane G. Improving OWC performance prediction using polychromatic waves. Energy 2015;93:1943–52. http://dx.doi.org/10.1016/j.energy.2015.10.086. Part 2.
[11] López I, Castro A, Iglesias G. Hydrodynamic performance of an oscillating water column wave energy converter by means of particle imaging velocimetry. Energy 2015;83:89–103. http://dx.doi.org/10.1016/j.energy.2015.01.119.
[12] Ning D-Z, Shi J, Zou Q-P, Teng B. Investigation of hydrodynamic performance of an OWC (oscillating water column) wave energy device using a fully nonlinear HOBEM (higher-order boundary element method). Energy 2015;83:177–88. http://dx.doi.org/10.1016/j.energy.2015.02.012.
[13] Falcão AFO, Henriques JCC. Oscillating-water-column wave energy converters and air turbines: a review. Renew Energy 2016;85:1391–424. http://dx.doi.org/10.1016/j.renene.2015.07.086.
[14] O'Sullivan D. Electrical generators in ocean energy converters. In: Alcorn R, O'Sullivan D, editors. Electrical design for ocean wave and tidal energy systems. Stevenage: The Institution of Engineering and Technology; 2013. p. 3–41.
[15] Budal K, Falnes J. Optimum operation of improved waver-power converter. Mar Sci Commun 1977;3:133–50.

[16] Babarit A, Duclos G, Clément AH. Comparison of latching control strategies for a heaving wave energy device in random sea. Appl Ocean Res 2004;26(5):227–38. http://dx.doi.org/10.1016/j.apor.2005.05.003.
[17] Babarit A, Clément A. Optimal latching control of a wave energy device in regular and irregular waves. Appl Ocean Res 2006;28(2):77–91. http://dx.doi.org/10.1016/j.apor.2006.05.002.
[18] Salter S, Taylor J. The design of a high-speed stop valve for oscillating water columns. In: Proc. 2nd European wave energy conf, vol. 3; 1996. p. 195–202.
[19] Hoskin RE, Nichols NK. Latching control for a point absorber wave-power device. Technical report NA1/86. Department of Mathematics, University of Reading; 1986.
[20] Hoskin RE, Count BM, Nichols NK, Nicol DAC. Phase control for the oscillating water column. In: Evans DV, Falcão AFO, editors. IUTAM symp. Hydrodynamics of ocean-wave energy utilisation. Springer-Verlag; 1986. p. 257–68.
[21] Jefferys R, Whittaker T. Latching control of an oscillating water column device with air compressibility. In: Evans DV, Falcão A F de O, editors. Hydrodynamics of ocean wave energy utilization. Berlin: Springer-Verlag; 1986. p. 281–91.
[22] Justino PAP. Pontryagin Maximum Principle and control of a OWC power plant. In: Proceedings of the 25th international conference on offshore mechanics and arctic engineering, Hamburg, Germany; 2006. p. 65–73.
[23] Henriques JCC, Falcão AFO, Gomes RPF, Gato LMC. Latching control of an OWC spar-buoy wave energy converter in regular waves. In: Proceedings of the 31st International Conference on Offshore Mechanics and Arctic Engineering, Rio de Janeiro, Brazil; 2012.
[24] Gomes RPF, Henriques JCC, Gato LMC, Falcão AFO. Hydrodynamic optimization of an axisymmetric floating oscillating water column for wave energy conversion. Renew Energy 2012;44:328–39. http://dx.doi.org/10.1016/j.renene.2012.01.105.
[25] Falcão AFO, Gato LMC, Nunes EPAS. A novel radial self-rectifying air turbine for use in wave energy converters. Renew Energy 2013;50:289–98. http://dx.doi.org/10.1016/j.renene.2012.06.050.
[26] Falcão AFO, Gato LMC, Nunes EPAS. A novel radial self-rectifying air turbine for use in wave energy converters. Part 2. Results from model testing. Renew Energy 2013;53:159–64. http://dx.doi.org/10.1016/j.renene.2012.11.018.
[27] Paparella F, Monk K, Winands V, Lopes M, Conley D, Ringwood J. Benefits of up-wave measurements in linear short-term wave forecasting for wave energy applications. In: Control applications (CCA), 2014 IEEE conference; 2014. p. 2048–53. http://dx.doi.org/10.1109/CCA.2014.6981604.
[28] Paparella F, Monk K, Winands V, Lopes M, Conley D, Ringwood J. Up-wave and autoregressive methods for short-term wave forecasting for an oscillating water column. Sustain Energy, IEEE Trans 2015;6(1):171–8. http://dx.doi.org/10.1109/TSTE.2014.2360751.
[29] Fusco F, Ringwood J. Short-term wave forecasting for real-time control of wave energy converters. Sustain Energy, IEEE Trans 2010;1(2):99–106. http://dx.doi.org/10.1109/TSTE.2010.2047414.
[30] Saupe F, Gilloteaux J-C, Bozonnet P, Creff Y, Tona P. Latching control strategies for a heaving buoy wave energy generator in a random sea. In: 19th IFAC World Congr, 19; 2014. p. 7710–6. http://dx.doi.org/10.3182/20140824-6-ZA-1003.00440. Part 1.
[31] Sheng W, Lewis A. Short-term prediction of an artificial neural network in an oscillating water column. Int J Offshore Polar Eng 2011;21(4):248–55.
[32] Abraham E, Kerrigan E. Optimal active control and optimization of a wave energy converter. Sustain Energy, IEEE Trans 2013;4(2):324–32. http://dx.doi.org/10.1109/TSTE.2012.2224392.
[33] Henriques JCC, Gomes RPF, Gato LMC, Falcão AFO, Robles E, Ceballos S. Testing and control of a power take-off system for an oscillating-water-column wave energy converter. Renew Energy 2016;85:714–24. http://dx.doi.org/10.1016/j.renene.2015.07.015.
[34] Henriques JCC, Gato LMC, Falcão AFO, Robles E, Faÿ F-X. Latching control of a floating oscillating-water-column wave energy converter. Renew Energy 2016;90:229–41. http://dx.doi.org/10.1016/j.renene.2015.12.065.
[35] Falnes J. Optimum control of oscillation of wave-energy converters. Int J Offshore Polar Eng 2002;12(2):147–55.
[36] Falnes J. Wave-energy conversion through relative motion between two single-mode oscillating bodies. J Offshore Mech Arct Eng (ASME Trans 1999;121:32–8. http://dx.doi.org/10.1115/1.2829552.
[37] Newman JN, Lee CH. Wamit user manual. 2004. available online at: http://www.wamit.com/manual.htm [Last accessed date 15.11.4].
[38] Perez T, Fossen TI. A Matlab toolbox for parametric identification of radiation-force models of ships and offshore structures. Model Identif Control 2009;30(1):1–15. http://dx.doi.org/10.4173/mic.2009.1.1.
[39] Dixon SL. Fluid mechanics and thermodynamics of turbomachinery. 4th ed. London: Butterworth; 1998.
[40] Falcão A F de O. Control oscillating-water-column wave power plant maximum energy Prod. Appl Ocean Res 2002;24(2):73–82. http://dx.doi.org/10.1016/S0141-1187(02)00021-4.
[41] Falcão AFO, Henriques JCC, Gato LM, Gomes RPF. Air turbine choice and optimization for floating oscillating-water-column wave energy converter. Ocean Eng 2014;75:148–56. http://dx.doi.org/10.1016/j.oceaneng.2013.10.019.
[42] Luenberger DG. Introduction to dynamic systems : theory, models, and applications. New York, Chichester, Brisbane: J. Wiley & Sons; 1979.
[43] W. H. Kwon, S. Han, Receding horizon control, Advanced textbooks in control and signal processing, Springer. doi:http://dx.doi.org/10.1007/b136204.
[44] Bryson AE, Ho Y-C. Applied optimal control: optimization, estimation, and control. Waltham: Blaisdell Publishing Company; 1969.
[45] Holthuijsen LH. Waves in oceanic and coastal waters. Cambridge University Press; 2007.